BNL-221080-2021-JAAM

Characterizing Hidden Structures at NSLS-II: Strongly Correlated Electron Systems, Functional Ceramics, Batteries, and Beyond

M. Abeykoon

To be published in "SYNCHROTRON RADIATION NEWS"

January 2021

Photon Sciences

Brookhaven National Laboratory

U.S. Department of Energy

USDOE Office of Science (SC), Basic Energy Sciences (BES) (SC-22)

DISCLAIMER

Characterizing Hidden Structures at NSLS-II: Strongly Correlated Electron Systems, Functional Ceramics, Batteries, and Beyond

Milinda Abeykoon, Eric Dooryhee, Michael Drakopoulos, Sanjit Ghose, and Zhong Zhong
Brookhaven National Laboratory, National Synchrotron Light Source II, Upton, New York, USA

Introduction

Brookhaven National Laboratory (New York) launched its high-energy X-ray science program at the inception of the National Synchrotron Light Source (NSLS), a U.S. Department of Energy (DOE) Office of Science User Facility. Built in the 1980s, the NSLS X17 beamline was the world's first super-conducting wiggler facility and remained in service for more than 30 years. The NSLS facility was decommissioned in October 2014 and a third-generation synchrotron machine, DOE's National Synchrotron Light Source II (NSLS-II), took over. Six years after completing construction, NSLS-II has a portfolio of 29 beamlines that includes two operating high-energy powder diffraction beamlines (XPD and PDF) and one high-energy imaging and diffraction beamline under construction (HEX).

The first part of this article reviews some of the milestones and achievements of NSLS and the transitioning of the high-energy X-ray science to NSLS-II. Part two presents a few recent case studies to emphasize the instrumentation and work that is being carried out at NSLS-II. Part three discusses the addition of a new beamline to NSLS-II's high-energy X-ray science program.

The onset of the high-energy X-ray science program at BNL

The initial drive for a high-energy capability at the NSLS was to enable medical imaging at the iodine absorption K-edge *in vivo*. The Synchrotron Medical Research Facility (SMERF) took its first human coronary artery images in 1990 [1]. In parallel, the multi-branch instrument X17 offered both monochromatic and white-beam capabilities and became the host of two other prominent programs: materials science research and high-pressure studies.

NSLS X17 took a seminal role in pioneering high-energy X-ray applications across the sciences and was highly influential on counterpart activities at other synchrotron facilities worldwide. Innovations include but are not limited to: (a) the development of diamond anvil cells (DACs [2] and large-volume, multi-anvil high pressure apparatus [3, 4] for studies of condensed matter under extreme conditions; (b) digital subtraction angiography on human subjects [1]; (c) multiple energy computed tomography for clinical research (e.g., in neurology and cardiology) [5]; (d) discovery and development of micro-beam radiation therapy for radiotherapy and radiosurgery of brain lesions [6]; (e) development of high-sensitivity phase-contrast imaging through diffraction enhanced imaging and analyzer based imaging [7]; (f) strain and phase mapping with energy-dispersive X-ray diffraction (EDXD) [8–10]; (g) reciprocal space mapping and diffuse scattering [11]; (h) computed micro-tomography (CMT) (e.g., on micrometeorites) [12]; (i) high-quality three-dimensional molecular structure from single-wavelength anomalous diffraction (SAD) phasing (e.g., a hen egg-white lysozyme using 56 keV photons near the Ho K-edge) [13].

For synchrotron monochromatic X-ray beams above 20 keV, conventional X-ray optics like sagittal bent Bragg crystals have intrinsic limitations. In the 2000s, the NSLS demonstrated the benefits of sagittal-focusing Laue optics suitable for high-energy photon beams [14, 15].

The high-energy X-ray capabilities at the NSLS were extended to another beamline, X7B, with a focus on *in-situ* studies of catalysts [16]. The high energies make it possible to access larger Q ranges, which stimulated the use of total scattering to determine the pair distribution functions (PDF) for materials [17]. New possibilities for defining PDFs of nano-materials at extreme conditions were also explored [18]. The high-energy science program is now being successfully continued at Brookhaven's new light source. The X-ray Powder Diffraction (XPD) and the Pair Distribution Function (PDF) beamlines at NSLS-II operate at energies ≥50 keV and use techniques and instrumentation pioneered at NSLS.

Real-time studies of novel reactive transformations using fast diffraction measurements

Synthesis of next-generation materials with targeted properties is optimized by understanding the reaction pathways. The scope of the materials synthesis research field is broad and includes functional materials for the production, conversion, and storage of energy, heterogeneous catalysts, new superconductors, semiconductors, or ceramics materials.

Decision making driven by solid-state chemistry and metathesis reactions has had some success in guiding exploratory syntheses [19, 20]. However, the discovery of new solid inorganic materials so far remains largely the result of either trial and error or serendipitous meth-

ods. Advancing beyond informed chemical intuition has often proven to be difficult, as the synthesis of solid-state materials involves the breakdown and reassembly of entire atomic lattices and not just a particular molecular entity. There is no mechanistic framework to describe these processes yet [21]. The strategy mainly consists in the difficult task of best-guess syntheses followed by characterization on post-mortem or recovered samples. As an alternative, materials discovery can be dramatically accelerated by using *in-situ* techniques [22, 23] in combination with theoretical calculations [24, 25]. The solid-state syntheses are explored using high-energy X-ray beam probes under different conditions, such as temperature, pressure, electromagnetic field, and reactive chemical processes. The formation of crystalline stable or metastable phases can be observed in real time, providing a record of the sequence of structures that occur during the chemical reaction. The final goal is to connect chemical knowledge, experimental data, and predictive theory and propose and test those reaction pathways that are the most promising for the synthesis of next-generation materials with targeted properties.

Here, we feature two examples of *in-situ* X-ray diffraction measurements (≥50 keV) at the NSLS-II to monitor solid-state reactions and phase transformations.

High-temperature flux synthesis

We investigated the synthesis of $La_2CuO_{4-x}S_x$ quaternary system by combining experimental and computational methods. La_2CuO_4 is the parent compound of the first high-temperature superconductor discovered within the cuprate family. Two new compounds, La_2CuO_3S and $La_2CuO_2S_2$ [26], can theoretically be derived by replacing half or all of the apical oxygens with sulfur in La_2CuO_4. La_2CuO_3S and $La_2CuO_2S_2$ are predicted to be thermodynamically stable in the short range but unstable in the long range [26]. In this study, *in-situ* XRD measurements are monitored to determine whether La_2CuO_3S and $La_2CuO_2S_2$ can actually form and, if so, by which synthesis route. The compounds are synthesized in a non-oxidative atmosphere inside an alumina tube inserted in a quadruple lamp furnace. High-energy X-rays with high flux are utilized to get fast diffraction patterns through the bulk of the sample and container, while heating up to 1100°C, followed by cooling (Fig. 1) [27]. The obstacle to forming these compounds is identified: a redox reaction between the Cu- and S-containing starting materials drives the synthesis away from the desired oxidation end-states. This incompatibility of the starting materials is also described by the DFT calculations. This study suggests that one could integrate theory and experiment in a closed loop for exploratory synthesis, where theory could identify theoretical desired materials that are thermodynamically stable, and *in-situ* XRD synthesis could be used to pinpoint the feasible synthetic pathways.

Electric field assisted reactive flash synthesis

Electric field assisted flash sintering has been recently discovered [28] and is now evolving into a mature process for the synthesis of multi-constituent ceramics, whose accurate composition is difficult to achieve by conventional methods. Powders of elemental components can be flashed in mere seconds and at low temperatures to produce single-phase oxides of complex compositions [29]. Phase transformation and sintering occur at the same time. One aim of this study was to control the rate of sintering, along with the rate of phase transformation. This was made possible by controlling the rate of the current during the flash, known as the Reactive Flash Sintering (RFS) method [30]. RFS can be employed for doping functional ceramics, such as ceramic electrolytes for lithium-ion batteries, and has the potential to hasten the discovery of new compositions with enhanced properties. RFS was successfully implemented in synthesizing the pure $BiFeO_3$ phase [31]

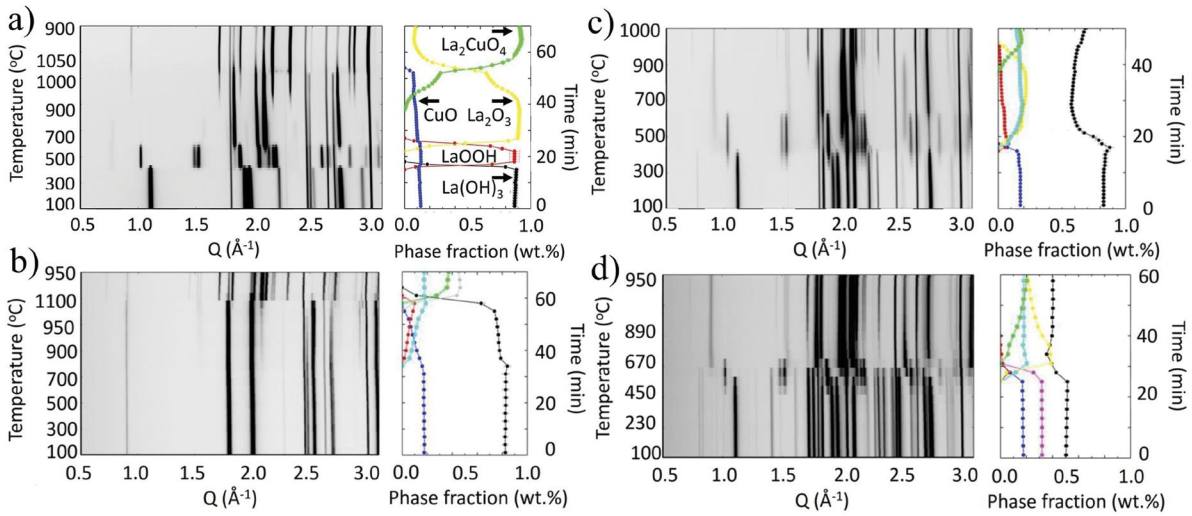

Figure 1: (a) Synthesis of La_2CuO_4 from La_2O_3 and CuO powders, monitored by in-situ powder XRD. (b) Synthesis of La_2CuO_3S from La_2O_2S + CuO. (c) Synthesis from La_2O_3 + CuS. (d) Synthesis from 2/3 La_2O_3 + 1/3 La_2S_3 + CuO. At left is shown the evolution of the diffraction peaks as temperature changes, and at right is shown the weight fraction of each phase determined from Rietveld refinements of the diffraction patterns [27].

and magnesium aluminate spinel ($MgAl_2O_4$) phase from powders of primary oxides [29]. The approach consists of optimizing the reaction process by synchronizing the rate of sintering with the rate of phase transformation, while monitoring *in situ* the XRD pattern.

The experiments were carried out with mixtures of three powders: magnesia, alumina, and zirconia. The *in-situ* synthesis/sintering was done at the NSLS-II using a newly built electric field assisted flash setup that accommodates different shapes and sizes of powder pellets. The reaction pathways and sintering processes were monitored *in situ* with fast, high-energy X-ray diffraction measurements [29, 30] (Fig. 2). We showed that the phase transformation of powders of magnesia and α-alumina into single-phase magnesium aluminate spinel was completed in 45 seconds, whereas sintering to full density required 60 seconds. We further observed that adding zirconia in the system worked as a catalyst, enhanced the conductivity of the system, and reduced the flash temperature [30].

Atomic modelling as a tool to uncover the physics of complex systems

Strongly correlated systems

As a result of coupling between charge, spin, orbital, and lattice degrees of freedom, strongly correlated materials exhibit rich properties, such as superconductivity, charge, spin, pair density waves [32, 33], pseudogap [34], frustrated magnetism [35], colossal magnetoresistance (CMR) [36], and metal-insulator transitions (MIT) [37]. A better understanding of the entanglement between properties and lattice degrees of freedom is necessary to enable their limitless applications, ranging from quantum computers to high-temperature superconductors. Emergence of these exotic properties is very often coupled to underlying lattice fluctuations. They are most of the time localized and hard to detect using conventional low-energy powder diffraction. High-quality diffraction data up to a large momentum transfer, coupled with total scattering studies, are necessary to detect the signal pertaining to these fascinating properties [38, 39].

$CuIr_2S_4$ is one such material that was studied at the NSLS-II [40]. A comprehensive structural study over an extended temperature range sheds light on the origin of local fluctuations at high temperature. CuIr2S[4] is one of the few systems that exhibit simultaneous charge ordering and spin dimerization at low temperatures [41]. The low-temperature insulating state of $CuIr_2S^4$ contains four-fold periodic Ir^{3+} ($5d^6$) and Ir^{4+} ($5d^5$) ions giving rise to Ir^{4+}- Ir^{4+} dimers, a classic example of tetrameric charge ordering [42]. The high-resolution PDF data clearly shows that these magnetic singlet Ir^{4+}- Ir^{4+} dimers disappear on warming through the MIT at 226 K (Fig. 3). The high-temperature cubic metallic phase contains $Ir^{3+}(5d^{5.5})$ partially occupied delocalized bands. However, high-resolution PDF data show that a symmetry-lowering orbital liquid-like state, the so-called d-orbital-degeneracy-lifted (ODL) state, exists up to 500 K. A study of the various chemical substitutions showed that the ODL state was electronically driven. This work further suggested that this phenomenon may be common among other partially filled degenerate d-electron systems. Another strongly correlated material studied at the NSLS-II is CsPbI3 [43]. High-resolution PDFs revealed the origin of room-temperature thermodynamic instability of the halide perovskite CsPbI3. The results show the rattling of the Cs atom between two split sites within the iodine coordination polyhedron above 150 K. This work also proposed methods to improve the stability of halide perovskite-based solar cells.

These studies would not have been possible without the use of high-energy X-rays to acquire PDF data up to a sufficiently high momentum transfer required to resolve barely separated interatomic distances resulting from local structural modulations. With the new addition of a 5T superconducting magnet coupled to a (5-500) K cryostat, the PDF beamline becomes the first beamline in the world to offer simultaneous magnetic field and temperature-dependent PDF, XRD, and SAXS capabilities.

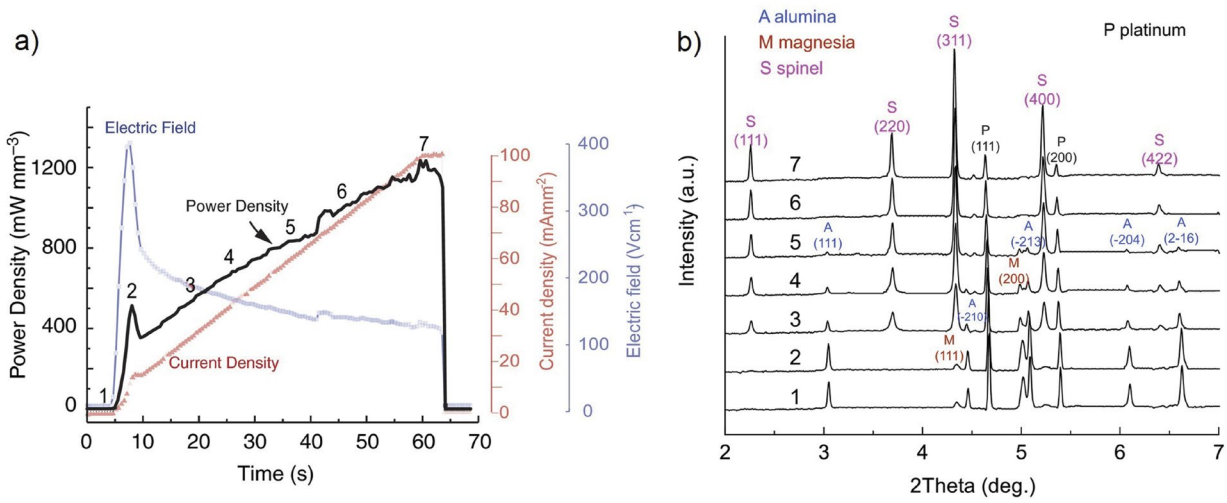

Figure 2: (a) Electric field, current density, and power density curves of the current rate flash experiment. Onset of the flash is signaled by a peak of voltage, around 10 s. (b) In-situ X-ray diffraction data of the composite with corresponding points from 1 to 7 in (A) [30].

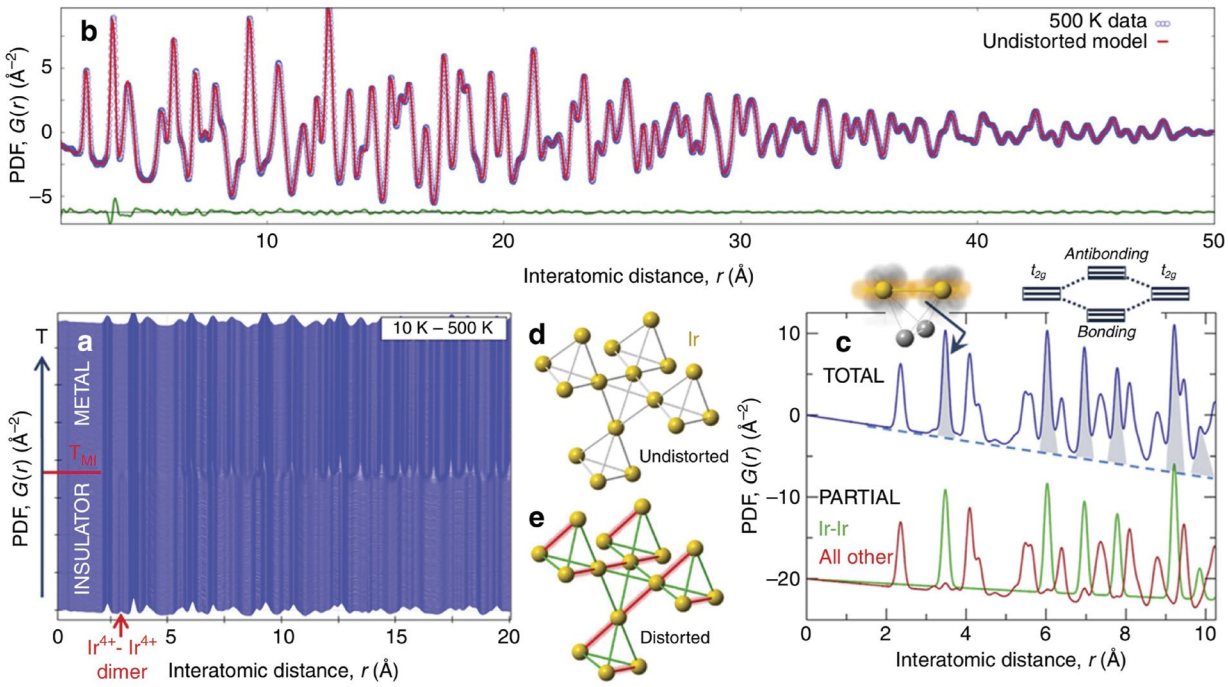

Figure 3: (a) Temperature-dependent PDF data on $CuIr_2S_4$, bottom (10 K), 2 K steps. (b) 500 K PDF fit using the cubic (Fd3m) model. Blue circles, red, and green solid lines represent measured data, model-based calculation, and fit residue, respectively. The misfit at ~3.5 Å corresponds to the signature of the ODL state. (c) Blue curve represents the calculated total PDF from high-temperature cubic (Fd3m) phase of $CuIr_2S_4$. The green curve represents the calculated partial PDF only using the Ir atoms in the structure. The red curve shows the calculated contribution from all other atoms in the structure. Shaded peaks in the total PDF highlight the Ir-Ir bond contribution that is sensitive to t2g orbital overlaps (sketched) and their spatial correlations. (d) Undistorted (cubic) and (e) high-temperature distorted (tetragonal) pyrochlore sublattices.

Nanomaterials

The potential applications of nanomaterials [44] depend on structural tunability and predictability. However, the lack of structural coherence in nanoparticles beyond a few tens of hundreds of atoms deters precise determination of their atomic structures using conventional low-energy powder diffraction. The finite size effects and the diffuse intensity, resulting from nanoscale structural disorder broadly distributed in the reciprocal space, call for total scattering techniques. The NSLS-II wiggler beamlines high photon energies, high fluxes and state-of-the-art fast area detectors with a suite of robust sample environments to study nanoparticle systems as well as the evolution of their structures during synthesis and/or processing.

In their recent work [45], Banerjee et al. used PDF fit residues from the attenuated crystal (AC) approximation to obtain quantitative information regarding nanoparticle shapes and their atomic structures. The AC approximation uses a spherical envelop function on a periodic unit cell structure to attenuate interatomic correlations at the particle boundary. The AC-based modeling has been successfully used to study the size, shape, broken symmetries, and even stacking faults [46, 47] in nanoparticle systems, with little or no attention paid to hidden information in the PDF fit residues. Fit residues from the AC approach are used here to determine the best particle shapes and atomic structures (Fig. 4). It is shown that rich structural information not only regarding particle shapes, but also regarding domain twining, is hidden in the fit residues. High-energy PDF data from multiple facilities, including NSLS-II, were used to demonstrate that the fit residues of metallic nanoparticle systems contain common features that were not instrument dependent. These features are intrinsic and originating from inadequate structure models. In a follow-up paper [48], a cluster mining approach was presented; in this case, libraries of nanoparticle models from various structural motifs were fitted and compared with experimental PDFs in order to select the best structural models. Similar approaches, combined with artificial intelligence algorithms, are currently being developed and integrated to data reduction workflows to predict potential structure models during measurements. Combined with the recently commissioned SAXS setup, the NSLS-II high-energy beamline are expanding their capability to study both the structure and morphology of nanoparticle systems.

A new high-energy beamline

The NSLS-II HEX beamline is currently under construction [49] and will be a powerful and versatile tool to advance materials in science and engineering. Typical samples to be studied include assembled and functioning batteries, photovoltaic materials, fuel cells, and a wide range of other engineering materials, such as gas turbine blades, composite structures, and materials under extreme conditions (stress, temperature, chemical environments, etc.). HEX will combine X-ray diffraction and imaging

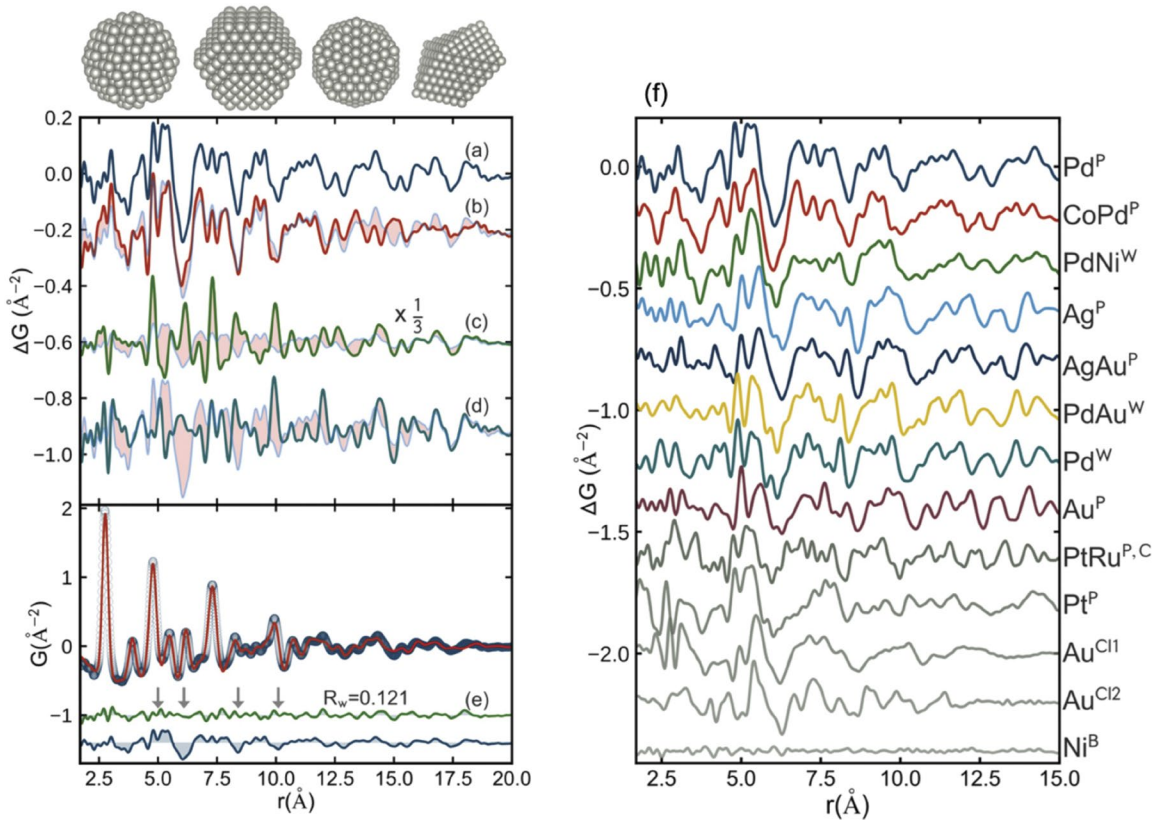

Figure 4: Fit residues from refinements of Pd nanoparticles using different particle types as shape functions: (a) spherical AC approach; (b) truncated fcc octahedron; (c) Mackay icosahedron (scaled by factor 1/3); (d) regular decahedron. The used cluster structures are shown above the panel in the same order from left to right (a-d). Light blue curves compare the scaled fit residue from AC approach with the fit residues from fittings based on models a-c. Left figure, bottom panel: blue circles, red, and green solid lines represent data, calculated PDF using a 3.6 nm decahedron, and the difference curve. The blue solid line represents the fit residue from AC approach using a spherical envelop function. (f) Comparison of common features among the fit residues resulting from AC approach fitting of various metallic nanoparticle systems.

tools with a monochromatic or a white beam to enable the study of real atomic structures under working conditions and in real time.

With the increasing adoption of electric cars, research is focusing on electrochemistry with the aim of increasing the power density of battery packs, and thus the efficiency and range of these vehicles. With increased power density, however, vehicles become more prone to battery failure and thermal runaway, which are often caused by impact or mechanical design flaws in the battery packaging. This calls for *in-situ* testing of the macro-system of commercial battery designs for mechanical integrity under conditions of overheating and uncontrolled disassembly [50]. Hard X-ray radiography with high time resolution offers unprecedented insight into the kinetics of such catastrophic failure modes and has been demonstrated in the past [51].

Commercial viability of novel battery designs depends on degradation behavior during long-term cycling. Morphological changes and phase changes can both lead to unwanted degradation. *Operando* monitoring of electrochemical kinetics, using high-energy X-ray diffraction (both ADXD and EDXD), is of great value. Anode and cathode materials degrade mechanically via the formation of strain cracks, which reduce conductivity. These can be visualized at the microscopic scale through high-resolution X-ray tomography *in situ* during formation [52].

The New York State Energy Research and Development Agency (NYSERDA) provided the funding for the development of this new NSLS-II facility. In order to penetrate thick metallic samples and sample environment of processing devices, the X-ray energy will range from 30 keV to 150 keV in monochromatic beam operation and over 200 keV using the white beam.

HEX comprises a superconducting wiggler, X-ray filtering, and a double crystal bent Laue monochromator, compatible with the large beam (typically $100 \times 20\,mm^2$) needed for imaging engineering samples. The downstream end station is housed in an external satellite building 100 m from the source and will be capable of running complex sample environments. Experiments will be performed with a variety of sample stages and with different detector setups for imaging, EDXD, and ADXD. Future upgrades include the addition of two side branches with end stations (Fig. 5).

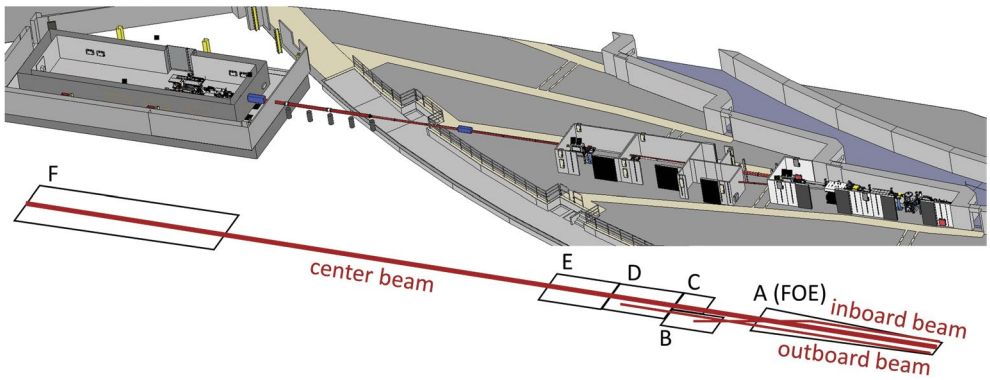

Figure 5: View of HEX beamline. Top: 3D-rendering. Bottom: Schematics of hutches (A-F) and the three wiggler beams (inboard, center, and outboard). Note that the inboard branch crosses the other two branches ending up in the B-hutch.

Detector technology is crucial at high energies due to the low attenuation in commonly used sensor materials. However, there is an advantage with short wavelengths, in that diffraction of atomic structures is confined into a narrow cone. Thus, area (2D) and strip (1D) detectors are most suitable for high-energy scattering and diffraction if they have sufficient quantum efficiency. Two recent developments promise to boost the efficiency of high-energy diffraction both for monochromatic and white X-ray beams using high-Z detection materials such as Germanium, CdTe, or GaAs. The latter two materials are used in area detectors for monochromatic diffraction, and some examples of commercially available devices can be found [53, 54]. Patterned Ge-wafers are used in a BNL design for energy-resolving multi-element detectors for EDXD or monochromatic work [55]. The small pitch of the individual detector elements allows advancement of the EDXD technique via a pinhole camera set up to detect more than 100 adjacent gauge volumes simultaneously.

Sample environments for *in-situ* experiments are important for conducting meaningful research. HEX will offer heavy-duty instrumentation with a versatile sample stage for diffraction and tomography, beam conditioning optics, and several detector supporting structures. This allows virtually any processing equipment to be positioned into the beam and investigated with the available synchrotron techniques. The implementation of customized sample equipment that research groups bring to the instrument will allow state-of-the-art *operando* experiments as close to the original setup at the home labs as possible.

Summary

NSLS-II supports three wiggler-based beamlines, namely PDF and XPD (in operation), and HEX (currently under construction), delivering high flux beams at high energies to observe and interrogate the local and average structures of dense or bulk materials in non-ambient or *operando* conditions. These high-energy X-ray beamlines are designed to examine the multi-scale structure (atomic scale to nm to μm to mm) of the materials across a wide spectrum of critical technologies, including applications with materials for the generation and storage of energy. The scientific focus areas of these instruments are:

- *In situ* synthesis and materials processing (e.g., high-temperature solid-state growth, growth of colloidal nanoparticles from solution, flash sintering of ceramics/oxide materials, nucleation and growth of MOFs, or microwave-assisted synthesis, structural transformations in additive manufacturing, solid-liquid interactions in melt-pools and alloy solidification, etc.);
- *In situ* and *operando* structure evolution (e.g., catalysis, oxidation-reduction reactions using gases, hydrogenation reactions, gas adsorption and separation, phase and structural transformation during cycling of energy storage devices, battery assembly failure, crack growth, strain, etc.);
- Combinatorial and high-throughput structure analysis (application to nuclear materials, energy materials, engineering materials, etc.);
- Solid-state physics: nanoscale structural fluctuations and hidden broken symmetry phases, structure and physical properties relationship (e.g., superconductors, magnetic transitions, quantum, thermoelectrics, negative thermal expansion, etc.).

Acknowledgments

The authors thank their colleagues—J. Hanson. D. Weidner, and L. Berman—for contributing their memories of the work performed at NSLS.

Funding

This article reports on research work carried out at the National Synchrotron Light Source (NSLS) and National Synchrotron Light Source II (NSLS-II). Both are U.S. Department of Energy (DOE) Office of Science User Facilities, operated for the DOE Office of Science by Brookhaven National Laboratory under Contracts No. DE-AC02-98CH10886 and No. DE-SC0012704, respectively. Full funding information can be found in the referenced papers. ■

References

1. W. Thomlinson et al., *Rev. Sci. Instrum.* **63**, 625–628 (1992).
2. H. Mao et al., *J. High Pressure Res.* **14**, 257–267 (1996).

3. Y. B. Wang et al., *Rev. Sci. Instrum*. **74**(6), 3002–3011 (2003).
4. D. Yamazaki et al., *Rev. Sci. Instrum*. **72**(11), 4207–4211 (2001).
5. X. Wu et al., *Rev. Sci. Instrum*. **66**, 1346 (1995).
6. D. Slatkin et al., *Medical Physics* **19**, 1395–1400 (1992).
7. Z. Zhong et al*., Nucl. Instrum. Meth. Phys. Res*. A **450**, 556–567 (2000).
8. M. Croft et al., *Int. J. Fatigue* **27**, 1408–1419 (2005).
9. J. Rijssenbeek et al *., Journal of Power Sources* **196**, 2332–2339 (2011).
10. K. Kirshenbaum, et al., *Science* **347**, 149–154 (2015).
11. H. Reichert et al., *Phys. Rev. Lett*. **87**, 236105 (2001).
12. S. R. Sutton et al., *Abstracts of the Lunar and Planetary Science Conference* **23**, 1393 (1992).
13. J. Jakoncic et al., *J. Appl. Cryst*. **39**, 831–841 (2006).
14. P. Suortti et al., *Nucl. Instrum. Meth. Phys. Res. A* **336**, 304–309 (1993).
15. Z. Zhong et al., *J Appl Cryst* **34**, 646–653 (2001).
16. M. Estrella et al., *J Phys Chem C* **113(**32**)**, 14411–14417 (2009).
17. K. M. O Jensen et al., *Nat Commun* **7**, 11859 (2016).
18. L. Ehm et al., *Appl Phys Lett* **98(2)**, 021901 (2011).
19. J. D. Corbett et al., *Inorg Chem* **39**, 5178–5191 (2000).
20. I. P. Parkin et al., *Chem Soc Rev* **25**, 199–207 (1996).
21. L. Soderholm et al., *APL Mater* **4**, 053212 (2016).
22. D. A. Kitchaev et al., *Nat Commun* **7**, 13799 (2016).
23. D. P. Shoemaker et al., *Proc Natl Acad Sci USA* **111(**30**)**, 10922–10927 (2014).
24. S. Curtarolo et al., *Nat Mater* **12**, 191–201 (2013).
25. R. Gautier et al., *Nat Chem* **7**, 308–316 (2015).
26. C. H. Yee et al., *Phys Rev B* **89**, 094517 (2014).
27. H. Hua et al., *Proc Natl Acad Sci USA* **115** (31), 7890–7895 (2018).
28. M. Cologna et al., *J. Am. Ceram. Soc*. **93**, 3556–3559 (2010).
29. B. Yoon et al., *J. Am. Ceram. Soc*. **102**, 2294–2303 (2019).
30. B. Yoon et al., *J. Am. Ceram. Soc*. **102**, 3110–3116 (2019).
31. E. Gil-González et al., *J Mater. Chem*. **6**, 5356–5366 (2018).
32. A. J. Achkar et al., *Nat. Mater*. **15**, 616–620 (2016).
33. F. Daniel et al., *Annu. Rev. Condens. Matter Phys*. **11**, 231–270 (2020).
34. I. Madan et al., *Nat Commun* **6**, 6958 (2015).
35. D. Billington et al., *Sci. Rep*. **5**, 12428 (2015).
36. Z. Qiu et al., *Nature Mater* **17**, 577–580 (2018).
37. R. Zhang et al., *Sci Rep* **8**, 17093 (2018).
38. A. M. Milinda Abeykoon et al., *Phys. Rev. Lett*. **111**, 096404 (2013).
39. K. R. Knox et al., *Phys. Rev. B* **88**, 174114 (2013).
40. E. S. Bozin et al., *Nat Commun* **10**, 3638 (2019).
41. P. G. Radaelli et al., *Nature* **416**, 155–158 (2002).
42. M. Croft et al., *Phys. Rev. B* **67**, 201102 (2003).
43. D. B. Straus et al., *Adv. Mater*. **32**, 2001069 (2020).
44. Y. Xia et al., *Acc. Chem. Res.* **46**, 1671–1672 (2013).
45. S. Banerjee et al., *J Phys Chem C* **122**(51), 29498–29506 (2018).
46. A. S. Masadeh et al., *Phys. Rev. B* **76**, 115413 (2007).
47. D. Hudry et al., *Chemistry of Materials* **28**(23), 8752–8763 (2016).
48. S. Banerjee et al., *Acta Cryst*. **A76**, 24–31 (2020).
49. https://www.bnl.gov/ps/beamlines/beamline.php?r=27-ID
50. J. Zhu et al., *Journal of Power Sources* **378**, 153–168 (2018).
51. D. P. Finegan et al., *Energy Environ. Sci.* **10**(6), 1377–1388 (2017).
52. X. Li et al *.,Electrochimica Acta* **297**, 1109–1120 (2019).
53. D. Šišak Jung et al *.,Powder Diffr.* **32**(S2), S22–S27 (2017).
54. https://x-spectrum.de/
55. A. K. Rumaiz et al., *IEEE Trans. Nucl. Sci.* **61**(6), 3721–3726 (2014).